Published in final edited form as:

Magn Reson Med. 2023 April ; 89(4): 1660–1673. doi:10.1002/mrm.29542.

Hybrid Active and Passive Local Shimming (HAPLS) for Two-region Magnetic Resonance Imaging (MRI)

Zhi Hua Ren[1], **Jason Stockmann**[2,3], **Andrew Dewdney**[4], **Ray F. Lee**[1]

[1]Zuckerman Mind Brain Behavior Institute, Columbia University, New York, NY, USA

[2]Athinoula A. Martinos Center for Biomedical Imaging, Department of Radiology, Massachusetts General Hospital, Charlestown, MA, USA.

[3]Harvard Medical School, Boston, MA, USA.

[4]Siemens Healthcare GmbH, Erlangen, Germany.

Abstract

Purpose: A MRI scanner is equipped with global shim systems for shimming one region of interest (ROI) only. However, it often fails to reach state-of-the-art when shimming two isolated ROIs simultaneously, even though the two-area shimming can be essential in scan scenarios, such as bilateral breasts or dyadic brains. To address these challenges, a hybrid active and passive local shimming (HAPLS) technique is proposed to simultaneously shim two isolated regions of interest areas within the whole FOV.

Methods: A local passive shimming (PS) system is constructed by optimized bilateral ferromagnetic chip arrays to compensate for the magnet's significant high-order B_0 inhomogeneities at the boundary of the manufacturer's specified homogeneous volume, thus locally improving the available FOV. The local active shimming (AS) consists of 40-channel DC loops powered by 64-channel current amplifiers. With the optimized current distribution, AS can correct the residual low-order B_0 inhomogeneities and subject-specific field inhomogeneities. In addition, AS is used to homogenize the center frequencies of the two regions.

Results: With the implementation of the HAPLS, the 95% pk-pk ppm was reduced from 1.92 to 1.12 ppm by 41.7%, and RMS decreased from 0.473 to 0.255 ppm by 46.1% in a two-phantom experiment. The volume ratio containing MR voxels within a 0.5-ppm frequency span increased from 64.3% to 81.3% by 26.3%.

Conclusion: The proposed HAPLS technique utilizes both passive and active local shimming, and it can efficiently shim two areas simultaneously which is an unmet need for a commercial MRI scanner.

Correspondence: Ray F. Lee, rl2946@columbia.edu.

CONFLICT OF INTEREST

Andrew Dewdney is an employee of Siemens Healthcare GmbH, Erlangen, Germany.

Keywords

Two-region MRI; High-order B_0 Inhomogeneity; Passive Local Shim (PS); Active Local shim (AS); Multi-coil Local Shim; Magnetic Field Susceptibility

INTRODUCTION

Global passive and active shimming systems in a state-of-the-art MRI scanner can effectively produce a single volume of the homogeneous static magnetic field ("B_0") in the empty bore within the 50-cm diameter sphere volume (DSV) centered at the bore's isocenter. Moreover, active spherical harmonic shim coils can partially compensate for subject-specific B_0 nuisance fields that arise from tissue susceptibility interfaces inside the body. However, in some clinical and functional MRI applications, simultaneously shimming two separate regions can be significantly more efficient, and in some cases even essential. For example, acquiring images of two knees[1] or two breasts[2,3], or two shoulders at once can reduce scan time by half if bilateral exams are required. Another example is studying two interacting human brains in one scanner simultaneously[4–6] where B_0 shimming of two side-by-side brains becomes imperative for acquiring EPI images, which are very sensitive to off-resonance effects. For two-area imaging, conventional MRI scanners' global active shimming (second-order spherical harmonic (SH) based shim coils) become ineffective for compensating the susceptibility-induced B_0 inhomogeneous fields inside each of the two brains. Moreover, some of the two-areas-to-be-imaged extend beyond the 50-cm DSV, and therefore suffer from extra high-order field inhomogeneities in the background magnetic field[7] that cannot be compensated by the scanner's conventional passive or active shims. The inability of simultaneously shimming two regions in commercial scanners results in image quality degradation or image distortions of two-area imaging[8].

So far, the B_0 field shimming research and practices can be attributed to two categories: passive shimming (PS) and active shimming (AS). The PS relies on the use of paramagnetic, ferromagnetic, and/or diamagnetic materials for field corrections. It is routinely used during the installation of a commercial MRI scanner, where an arrangement of ferromagnetic plates will be optimized iteratively and inserted into sliding trays along the inner bore of the magnet to reduce the magnet inhomogeneities[9–11]. Besides shimming the magnet inhomogeneities, more localized PS techniques are also capable of correcting the subject-specific susceptibility inhomogeneities[12–15]. For example, the placement of diamagnetic material (pyrolytic graphite) with an optimized geometry in the mouth can reduce the susceptibility artifacts caused by the inferior frontal cortex (IFC)[12]. Using more than one type of material in PS can increase the flexibility to generate the high-order terms of shim fields to correct susceptibility-induced field distortions[15]. However, to adapt to the subject-dependent susceptibility inhomogeneities, the mass, geometries, and/or locations of the magnetic materials have to be adjustable to generate the optimal compensating fields. Altering the scanners' PS requires ramping down the magnet, which is not feasible for a routine scan, so PS is usually locally applied to deal with the susceptibility-induced field distortions. In 2011, S. Yang et. al presented a local passive shimming method with an adjustable positioning assembly to deal with the subject-specific

inhomogeneities in the prefrontal and temporal regions[16]. The locations of the four Niobium cylinders were adjusted based on the optimization routine and experimental results iteratively to get the optimal shim. It was also demonstrated that PS can shim multiple imaging volumes simultaneously, or selected targeted imaging volume with a tailored optimization algorithm[17,18]. Overall, the PS is capable of correcting high-order terms of field inhomogeneities with its flexibility on the mass, geometry, locations, and magnetic properties of the material used. It has no power consumption, no heat dissipation, and is relatively low in cost. However, when accounting for the subject-to-subject variants of the susceptibility-induced inhomogeneity, the rearrangement of the distribution of shim materials will be time-consuming, and the design of a fixture to hold the magnetic material robustly with adaptive flexibility will be challenging.

Active Shimming (AS) is implemented by using the conductor loop/loops carrying currents to generate the compensating magnetic fields. Generally, resistive shim coils are used for active shimming. The superconducting shim coils that are sometimes built-in commercial MRI scanners with 3T and above can perform shimming up to the third order[9]. However, the currents flowing in the superconducting coils cannot be adjusted easily after the shimming during MRI scanner installation, so they are intended only for shimming the empty bore of the magnet. There are also resistive AS used for targeted region/regions within the empty DSV[19]. In this paper, the AS refers to using resistive shim coils that are intended to compensate for in vivo $\boldsymbol{B_0}$ inhomogeneity on a subject-specific basis[20–28]. Recently, several studies have shown the feasibility of combining the Rx/Tx with active shim (iPRES)[29], or active shim and RF reception (AC/DC array) with the same conductive loops in a coil array[24–27], where inductive chokes are used to bridge the tuning capacitors for a single-turn loop. Prior works have shown that AS can handle low-order (up to third order) shimming well, but is limited in its ability to compensate higher-order B_0 fields due to the limited number of loops used in which higher-order terms become very inefficient, so matrix coil approaches are used[30]. There are also attempts to combine both PS and AS to shim small-bore B_0 fields[20,31]. In Ref. 20, both passive and active shimming were used simultaneously to shim the macaque's visual cortex (around 5×5×5 mm^3) for in vivo MR spectroscopy at 7T, and PS was used to generate second-order shim fields, while the AS handled the residual field inhomogeneities. Overall, AS typically generates lower-order field terms while it is relatively easy to adjust the current distributions.

To address the challenge of two-region MRI, a hybrid active and passive local shimming (HAPLS) technique is proposed to shim two isolated regions within one large FOV simultaneously by taking advantage of both PS and AS[32]. A localized PS is used first to extend the usable FOV within sub-regions of the bore by shimming the background B_0 field up to a high spatial order, neglecting any concomitant deterioration in homogeneity that will occur outside of these sub-regions as they are of no interest for this application. The AS is then used to homogenize the center frequencies of two regions which may be shifted differently after optimizing PS in two areas. Furthermore, AS will deal with the residual field inhomogeneities and the additional subject-specific field inhomogeneities. The AS and PS are thus mutually complementary in the proposed method. While we expect the proposed technology to benefit in vivo shimming of two regions (such as two breasts, two shoulders,

or dyadic brains) simultaneously in the bore, the scope of the present study is focused on improving background B_0 homogeneity in the magnet bore; however, our results suggest that the HAPLS technology will locally improve in vivo B_0 homogeneity as well.

METHODS

The Initial B_0 Field and the Built-in Shimming

All simulations, optimization, and experimental validation were performed on a 3T Siemens Healthineers MAGNETOM Prisma scanner (Siemens Healthcare GmbH, Erlangen, Germany). The initial B_0 established during the scanner installation was measured by a vendor-provided "Array Shim Device" which consists of 24 magnetic field sensors arranged around the perimeter of a 50-cm diameter circular plate. During the field measurements, the plate was rotated 20 times with rotation angle increments of 18°. The final measurement data consisting of all 480 points on the 50-cm DSV was then decomposed to up to 23th-order spherical harmonics,

$$B_Z(r,\theta,\varnothing) = \sum_{n=0}^{23}\sum_{m=0}^{n}(A_n^m cos\cos(m\varnothing) + B_n^m sin\sin(m\varnothing))P_n^m\cos(\theta) \quad (1)$$

Where, $B_Z(r,\theta,\varnothing)$ is the B_Z field at the observation point r, θ, $\varnothing$ in a spherical coordinate system, n and m are the order and degree of the SHs, respectively, A_n^m and B_n^m are the weighting constants for corresponding SHs, and $P_n^m\cos(\theta)$ is the associated Legendre functions. Figure 1(a) shows the field on the surface of 50-cm DSV based on measurement. Among the 23 axial orders of SHs, the top three dominant SH terms of the expansion of the B_0 field within 50-cm DSV are all high-order ones – a(12,0), a(14,0), and a(8,0), and they are at 12.3, 5.84, and 1.94 (in ppm), respectively.

In this work, the two areas targeted for B_0 shimming are shown in Figure 1(b). It is challenging because: (1) the background B_0 field in both areas contains up to 16thorder SH field inhomogeneities; (2) the scanner's built-in SH-based in vivo shim routines are designed for one volume, so it cannot effectively shim two off-center volumes simultaneously and optimally. The magnetic fields of the two areas in the initial B_0 condition (Tune-up shim setting established during scanner installation) are shown in Figure 2(a). Here, it is assumed that the first- and second-order spherical harmonics distortions are perfectly eliminated over the 50-cm DSV. The B_0 fields of the two areas show distinct left-right asymmetry and steep spatial variations in regions close to the bore of the scanner. The peak-to-peak (pk-pk) ppm for the two are 3.39 ppm and 8.92 ppm respectively. When two home-made 20-cm spherical $CuSO_4$ phantoms were placed in the two targeted areas, after running the scanner's automatic shimming routine, the B_0 fields of two areas are shown in Figure 2(b). This demonstrated that the built-in second-order SH shimming not only cannot handle the localized high-order (up to 16th order) inhomogeneity but also only focused on the left region (−x), and negligible improvement on the right region (+x). Furthermore, the center frequencies of the two regions were separated by about 60 Hz after automatic SH shimming as shown in Figure 2(c).

Localized Passive Shimming

In the proposed method, the local passive shimming is better focused to compensate for the high-order, highly-localized B_0 field inhomogeneity. Passive shimming is implemented by affixing a ferromagnetic chip array (VACOFLUX 50, VACUUMSCHMELZE GmbH & Co. KG, Germany) surrounding the two target areas with optimized chip thicknesses and locations. To generate high-order shim fields, two arrays of high-spatial-resolution pockets for affixing shim chips are defined on the surface of a cylinder (aligned with the scanner's axial axis) with a diameter of 582 mm as shown in Figure 3(a) (predefined locations for all pockets are summarized in Table 1). Note that there are no pockets allocated in regions from −30 mm to 30mm along the z-axis, since ferromagnetic chips in this region will tend to exaggerate the field distortions therein. This geometry was also chosen to match the spatial variation of the magnet's design SHs to the spatial distribution of the dipole fields induced by the shim chips and is more efficient than following the contours of the shim coils or placing the chips very close to the sub-regions. All shim chips affixed in the shim pockets have the same area of 5×5 mm^2 to keep a relatively constant volume magnetization and allow a standard calibration, and the thickness of shim chip stacks at each location will be optimized to correct field distortions.

To calculate the magnetic field generated by a ferromagnetic chip, first, a current model is applied to reduce the magnetized shim chip to equivalent surface currents[33–35] then the Biot-Savart Law is used to compute the magnetic field of the chip. When a ferromagnetic chip is placed inside the bore of the 3T MRI scanner, it will achieve saturated magnetization. According to the specifications of the ferromagnetic material, the shim chip will be acting equivalently like small magnets with a remanence of 2.064T and aligned with the B_0 field (z-direction). Based on the current model, the magnetic field generated by the chip can be calculated by

$$\vec{B}(\vec{r}) = \frac{\mu_0}{4\pi}\oint_S \vec{j}_m(\vec{r}') \times \frac{\vec{r} - \vec{r}'}{|\vec{r} - \vec{r}'|^3} ds' \quad (2)$$

Where, μ_0 is the permeability of the free space, $\vec{r} = (x, y, z)$ is the observation point, $\vec{r}' = (x', y', z')$ is the point of the current source, $\vec{j}_m$ is the equivalent current source, and S is the surface of the magnet. The equivalent surface currents of a unit shim chip (Supporting Information Figure S1) were shown in Supporting Information Equation S1. As all the shim chips are magnetically saturated, the superposition principle holds. Overall, the summation of the field generated by all shim chips gives the total shim field generated by the PS chip array.

For the optimization of the passive shim, the area of the chip and pocket locations are all predefined and unchanged, and the thickness T_i of the i^{th} chip stack is taken as the variable to be optimized. There are 440 chip stacks in total under optimization, and the range of thickness is set to be 0–1.2 mm with an increment of 0.05 mm. To accelerate the forward calculation for the optimization, the field generated by one unit chip (5mm x 5mm x 0.05mm) was calculated and saved in MATLAB (MathWorks, MA, USA).

The optimization of the passive shimming is conducted by a genetic algorithm for its flexibility and the potential of providing high-diversity solutions in MATLAB[36]. Given that the two target areas have different initial B_0 fields, the left and right target areas are optimized separately. Their fitness functions are defined to minimize the root mean square (RMS) of the field on spherical surfaces of both target areas respectively as following

$$f_{(1}(T_L) = \sqrt{\frac{1}{N_L}\cdot\sum_{i=1}^{N_L}\left(B_{z_L}^i(X_L^i,T_L)-B_{0_{Int}}(X_L^i)\right)^2} \quad i=1,2,\cdots,N_L \tag{3}$$

$$f_2(T_R) = \sqrt{\frac{1}{N_R}\cdot\sum_{i=1}^{N_L}\left(B_{z_R}^i(X_R^i,T_R)-B_{0_{Int}}(X_R^i)\right)^2} \quad i=1,2,\cdots,N_R \tag{4}$$

Where, T_L and T_R are the thickness matrices of the left and right shim chip array under optimization, X_L^i and X_R^i are coordinates of the i^{th} voxel on spherical surfaces of the left and right target area, N_L and N_R are total numbers of voxels in left and right target areas, $B_{0_{Int}}$ denotes initial B_0 fields, and $B_{z_L}^i(X_L^i,T_L)$ and $B_{z_R}^i(X_R^i,T_R)$ are PS fields generated at X_L^i and X_R^i after applying the PS with the distribution of T_L and T_R, respectively. Note that optimizing two target areas separately can achieve optimal passive shimming in the two regions, however, it may result in two different center frequencies of magnetic fields in two target areas, which can be commensurate with the active shimming.

To implement the passive shimming, an acetal holder was designed and fabricated using a CNC machine (shown in Figure 3b)). The fixture to affix shim chips was printed by a 3D printer (Raise3D Pro2 Series, CA, USA) with polycarbonates (PC). There are three different thicknesses with the PS chips: 0.05 mm, 0.1 mm, and 0.3 mm. All shim chips were cut into a piece with an area of 5×5 mm^2 by a bench shear, and chips were stacked to get the optimized thicknesses and placed in corresponding pockets.

Localized Active Shimming

To implement the active shimming, a shim current supply system based on class-AB amplifier circuits was constructed and shown in Figure 4(a)[37,38]. It supports up to 64 channels of active shimming, and up to ±2.5 A per channel with a water-cooling system (Lytron, Woburn, MA) to accelerate heat dissipation. The shim current supply system is controlled by a Teensy 3.5 microcontroller via fiber cables. When implementing the AS, the current distribution was firstly optimized offline, and then uploaded to the microcontroller which will send serial peripheral interface (SPI) bus commands to the current supply system when triggered by manual commands or TTLs from the scanner. To work with the current supply system, a 40-channel bilateral local AS coil array was designed and constructed as shown in Figure 4(b), and the layout of the coil elements is illustrated and labeled as shown in Figure 4(c). Each side of the bilateral AS coil array has 4×5 elements, and each element was made of AWG 18 magnetic wire and had a number of turns of 3, it was wound around a 10-mm thick coil fixture with an area of about 76×70 mm^2. Every 4×5 elements were affixed on the surface of a 3D-printed 120°-arced holder with an outer diameter of 175 mm. One pair of high-inductance house-made toroid RF chokes were added at the feed port of each shim coil to suppress the eddy currents induced by gradient coils and reduce the

interference to the body coil. All the chokes were fixed by screws on the coil fixture to avoid the mechanical vibration caused by gradient fields. The bilateral shim coil arrays were mounted to a wooden frame with a space of about 240 mm between two center points, and two 20-cm phantoms will be placed on holders on the frame. Each side of the AS coil array is terminated with an ODU connector supporting up to 45 channels (ODU-MAC ZERO, ODU GmbH & Co. KG, Germany), and interfaced to the current supply system through two multi-pair cables (25-pair twisted, Alpha Wire Co, NJ, USA) terminated with counterpart connectors to AS coils and current supply system. To suppress the RF interference and eddy currents induced during the scan, house-made floating cable traps were clamped to multi-pair cables[39].

To acquire volumetric field maps of each shim coil, the double-echo gradient-echo field mapping sequence was performed with ±0.5 A for each channel. During imaging, the built-in shimming in the prescan was bypassed, so that the background B_0 field is based on the default system tune-up shim. When getting the shim field map of each shim coil, shim coils with phantom were placed relatively close to the isocenter of the scanner to avoid the effect caused by the nonlinearity of the gradient field at regions close to the scanner bore. The subtraction of the field maps at ±0.5 A was made to eliminate the effect of the background field, so the field map of each coil element generated by the unit current (1 A) can be obtained and ready for the optimization of the current distribution for 40-channel active shim coils.

The optimization of the active shim is conducted on the B_0 field after PS, where the high-order inhomogeneities have been largely removed. Its fitness function is defined by

$$f_3(I) = \sqrt{\frac{\sum_1^{N_L}\left(B_{z_L}^i(X_L^i,\ I)\ -\ B_{Z_P}(X_L^i,\ T)\right)^2\ +\ \sum_1^{N_R}\left(B_{z_R}^i(X_R^i,\ I)\ -\ B_{Z_P}(X_R^i,\ T)\right)^2}{N_L\ +\ N_R}} + R\left(\left|B_{CTR_L}^{HAPLS} - B_{CTR_R}^{HAPLS}\right|\right) \quad (5)$$

Where, I is the current distribution under optimization for all 40-channel active shim coils, $B_{z_L}^i(X_L^i, I)$ and $B_{z_R}^i(X_R^i, I)$ are the fields derived from AS at X_L^i and X_R^i with the current distribution I, $B_{Z-P}(X_L)$ and $B_{Z-P}(X_R)$ are the B_0 field after PS within left and right sub-FOVs, respectively. $B_{CTR_L}^{HAPLS}$ and $B_{CTR_R}^{HAPLS}$ denotes the center frequency of B_0 fields in two target areas after both AS and PS. The first term on the right side of Equation 5 is to optimize the current distribution of AS. The second term $R\left(\left|B_{CTR_L}^{HAPLS} - B_{CTR_R}^{HAPLS}\right|\right)$ is a regularization (penalty term) of the optimization, and it will penalize the fitness value when the difference between center magnetic fields of both target areas is larger than 0.1 ppm. The fitness function in Equation 5 is minimized by a nonlinear constrained optimization algorithm (fmincon) in MATLAB to get the optimal current distribution. There are 40 channels in total, and the range for each is [−2.5A 2.5A] for a constrained optimization.

RESULTS

Passive Shimming

In the numerical simulation, the genetic optimization routine for passive shim was repeated several times and converged to a group of results showing similar shim performance. One of

the optimized distributions of the PS chip array was shown in Figure 3, and it also showed the simulated B_0 field after the passive shim on the spherical surfaces of two target areas. The detailed locations and dimensions of the optimized passive shim array are summarized in Table 1. Compared to the B_0 field before the passive shim, the RMS on the spherical surfaces of the two areas was reduced from 0.67 ppm to about 0.388 ppm by about 42.1%. It also brought the pk-pk ppm from 8.94 ppm to about 3.47 ppm by 61.2%. The B_0 field before the passive shim, the shim field generated by the passive shim, and the B_0 field after the passive shim are shown in Figure 5. The shim field shows a reversed pattern of high-order distortions compared to the initial B_0 field, which cancels out the initial B_0's high-order inhomogeneity and yields lower-order inhomogeneous B_0. The assembly of the passive shim fixture with shim chips is shown in Figure 3(b).

The numerical optimization results of passive shim were validated with experiments. Two aforementioned custom-made phantoms were used to measure the B_0 field before and after the passive shim. The field maps were acquired with the double-echo gradient-echo field mapping sequence, and field maps before and after the PS are present in Figure 6 (a) and (b), respectively. As shown in Figure 6(a), the B_0 field without the PS is more inhomogeneous compared to that shown in Figure 2(a), this is mainly due to magnetic susceptibility effects. The phantom is made up of two 3D-printed hemispherical shells (PC) and the gap is filled with epoxy resin and held together tightly by screws, and the interior surface of the phantom shell is also covered by one thin layer of epoxy resin to reduce the leakage and evaporation of the $CuSO_4$ solution. The discontinuities among $CuSO_4$ solution, air bubbles, epoxy resin, and PC phantom shells resulted in susceptibility-induced inhomogeneities within two target areas. Although magnetic susceptibility effects were not taken into account during the optimization of the PS, the experimental volumetric RMS was still reduced from 0.55 ppm to 0.4 ppm by about 27.3%, and the 95% pk-pk ppm decreased from 1.92 ppm to 1.51 ppm by about 21.4%. Above all, the high-order inhomogeneities shown in transversal xy-planes were greatly reduced. For the subject-dependent susceptibility inhomogeneities, for example, those at regions close to the top and bottom of the phantom due to air bubbles and epoxy resin, the PS didn't address them and left them to the AS.

Passive and Active Shimming

The optimization of AS is based on the field after the PS shown in Figure 6. The current distribution after optimization is shown in Figure 7 (a). The optimized current distribution was then uploaded to the microcontroller and the currents were applied to the active shim coil array to perform the HAPLS. The experimental setup of the HAPLS was shown in Figure 7(b), and the B_0 field after applying HAPLS is shown in Figure 7(c). After applying HAPLS, experimental results showed that the standard deviation (SD) of the B_0 field decreased from 0.39 ppm (with only PS) to 0.28 ppm by 28.2%, and the 95% pk-pk ppm decreased from 1.43 ppm (with only PS) to 1.12 ppm by 21.7%.

Comparing the field pattern after passive shim in Figure 6, the quasi-linear gradients in the central parts of both target areas are reduced to the relatively homogeneous field, and the B_0 fields in most of these areas are within 0.5 ppm as shown in Figure 7(c). Moreover, the high-order inhomogeneous field areas (regions close to the scanner bore) were significantly

improved. These changes can be illustrated by the plot of the B_Z field along the center x-axis (y = 30 mm) of both target areas shown in Figure 8(a). The non-linearity of the B_Z field along the x-axis was significantly reduced. The histogram plot of all the field inhomogeneities within both target areas was shown in Figure 8(b). Compared to the field distributions shown in Figure 2(c), it is evident that HAPLS significantly outperforms the scanner's built-in shimming routine. It can simultaneously shim two target areas, whereas the scanner's built-in shimming routine cannot. The volume ratio containing MR voxels within a 0.5-ppm frequency span was increased from 64.3% to 81.3% by about 26.3%. Overall, compared to no shim, the 95% pk-pk ppm was reduced from 1.92 ppm to 1.12 ppm by about 41.7%, and the RMS decreased from 0.473 ppm to 0.255 ppm by about 46.1% with the implementation of the HAPLS.

DISCUSSIONS

The passive shimming successfully reduced the high-order field distortions both in simulation and experiments. Only ferromagnetic material with strong magnetization was utilized in the present work, other types of magnetic material can be introduced to increase the flexibility of the passive shimming, such as pyrolytic carbon (diamagnetic material) with a negative susceptibility up to about −450 ppm[14,40]. The diamagnetic material could primarily fill up the [−30 mm 30 mm] region along the z-axis to provide more possibilities for the optimization of PS.

The constructed active shim coil array covers only partial angles of the bi-focal FOVs, which is mainly targeted to shim regions close to the scan bore. When mapping the field within home-made phantoms, additional field inhomogeneities were introduced by the air inside the phantom (+y top region), gaps in the middle of the phantom shell, and discontinuous boundaries between $CuSO_4$ solution and 3D-printed phantom shell (Polycarbonate) which is coated with epoxy resin inside. Those inhomogeneities close to +y and −y regions are out of reach of the bilateral active shim array, thus those low-order field inhomogeneities could not be well corrected. The performance of the active shimming can be enhanced with an active shim array covering larger angles and areas.

Regularization of both local shim volumes is critical since the background B_0 field is intrinsically left-right asymmetric. Although the introduction of the ferromagnetic chips can help reduce the high-order spherical harmonic components, they will alter the center Larmor frequency (average Larmor frequency) of two sub-FOVs differently due to only ferromagnetic materials used and different amounts of chips used for two sub-FOVs in the present work. The introduction of active shimming could regularize the central frequency of both sub-FOVs while shimming the residual inhomogeneities, for the current direction could be easily reversed in the loop array.

The present work demonstrated volumetric shimming for both passive shim and active shim. The passive shim is not adjustable during the scan in the present work, while the constructed current supply system is capable of updating the currents in active shim coils in synchronization with pulse sequences. Previous work has shown that slice-based shim can significantly boost shimming performance compared to volumetric shimming[24].

For slice-optimized dynamic shimming, TTL pulses supplied by the scanner trigger the microcontroller to send SPL bus commands to power amplifier boards before the beginning of each TR. The hardware presented is capable of performing slice-based dynamic shimming, and this will be investigated next.

The proposed HAPLS method can be used as a complementary shimming technique for two-region MRI such as breast and shoulder MR imaging. For example, the quality of breast MR imaging highly relies on the shimming performance, such as the homogenous fat suppression which requires good shimming regarding susceptibility-induced inhomogeneity[41]. A typical scan routine images the breasts sequentially, which is time-consuming. Some scanners provide one additional shimming FOV for breast imaging, however, the variability of the parameter adjustment by the technologists is experience-dependent and can affect the shimming output and image quality significantly[2]. It is even more challenging to shim the two-voxel MR spectroscopy for two breasts simultaneously[42]. The HAPLS approach can improve bilateral breast MRI/MRS significantly, although it will require different designs and optimizations for different applications and FOVs. When the proposed concept of HAPLS is applied to two-breast imaging, not only the two targeted imaging regions will be lower along the y-direction, but also the AS coil array design will be different since the orientations of two breasts and two brains are 90-degree apart. The size of the two sub-FOVs may change as well, and the distribution of PS chips will need to be relocated and re-optimized for breast MRI, and the holder of fixture of the passive shim chips will also be redesigned accordingly.

The ultimate goal of the HAPLS is to be applied in dyadic fMRI for studying two interacting brains inside one scanner[4,5]. Without local shimming, parts of the occipital lobes of two subjects fell into the high order B_0 inhomogeneous regions closed to the scanner bore, which results in significant SNR reduction, and the visual cortex area in many medium-sized heads was truncated. With the HAPLS system in a commercial MRI scanner, both brains will be in the B_0 fields that are homogenous enough for the EPI sequences to acquire complete dyadic brain functional data. To demonstrate the capability of the proposed HAPLS method for shimming two brains in dyadic fMRI, we collected the 3D B_0 maps of two brains within two targeted imaging regions using scanner's body coil, and then applied HAPLS to them. The experiment was approved by the Institutional Review Board of Columbia University (IRB AAAR7102). The B_0 field in two brains within two targeted imaging regions before and after applying HAPLS is shown in Figure 9. The PS is the same as that shown in the manuscript, and the AS was re-optimized. The figure below shows the B_0 field in transversal and coronal planes before and after HAPLS, respectively. With HAPLS, the RMS within two brains decreased from 0.461 ppm to 0.211 ppm by about 54.2%, and the 95% pk-pk ppm was reduced from 1.54 ppm to 0.87 ppm by 44%. Noted that the regions close to the isocenter of the scanner were not improved too much, which is due to that the 40-ch AS coil array is more confined on two sides (+x and −x regions), thus the isocenter of the scanner is hard to reach. In the dual-head AC/DC coil array we are building, both local FOVs will be 360-degree surrounded, and a better shim performance will be expected.

CONCLUSION

The hybrid active and passive local shimming was proposed to shim two-region MRI studies with high-order B_0 field inhomogeneities where conventional SH shimming is unable to achieve the required improvements. The passive shim focuses more on locally improving the high-order field inhomogeneities which are an intrinsic property of the scanner type and generally not affected by the manufacturer's passive shimming, whilst the active shim concentrates mainly on the residual low-order terms and magnetic susceptibility effects. Both the simulation and experimental results validated the feasibility of the proposed method. More systematic experimental design and optimization will prepare the proposed approach for the in vivo dyadic fMRI scan in the near future.

Supplementary Material

Refer to Web version on PubMed Central for supplementary material.

ACKNOWLEDGEMENT

The authors would like to thank for the grants from NSF 1926789 and NIH U24EB028984, also thank the support from Bernd Stoeckel.

RERFERENCE

1. Kogan F, Levine E, Chaudhari AS, et al. Simultaneous bilateral-knee MR imaging. Magn Reson Med. 2018;80(2):529–537. doi:10.1002/mrm.27045 [PubMed: 29250856]
2. Zhou W, Favazza CP, Axmacher JA, Trzasko JD, Geske JR, Lee CU. Evaluation of Shimming Techniques on MRI Breast Image Quality at 1.5T. J Breast Imaging. 2019;1(3):199–204. doi:10.1093/jbi/wbz045
3. Harvey JA, Hendrick RE, Coll JM, Nicholson BT, Burkholder BT, Cohen MA. Breast MR Imaging Artifacts: How to Recognize and Fix Them. RadioGraphics. 2007;27:131–146.
4. Lee RF, Dai W, Jones J. Decoupled circular-polarized dual-head volume coil pair for studying two interacting human brains with dyadic fMRI. Magn Reson Med. 2012;68(4):1087–1096. doi:10.1002/mrm.23313 [PubMed: 22213428]
5. Lee RF. Dual logic and cerebral coordinates for reciprocal interaction in eye contact. PLoS One. 2015;10(5):1–23. doi:10.1371/journal.pone.0121791
6. Renvall V, Kauramäki J, Malinen S, Hari R, Nummenmaa L. Imaging Real-Time Tactile Interaction With Two-Person Dual-Coil fMRI. Front Psychiatry. 2020;11(April):1–11. doi:10.3389/fpsyt.2020.00279 [PubMed: 32116830]
7. Koch KM, Papademetris X, Rothman DL, De Graaf RA. Rapid calculations of susceptibility-induced magnetostatic field perturbations for in vivo magnetic resonance. Phys Med Biol. 2006;51(24):6381–6402. doi:10.1088/0031-9155/51/24/007 [PubMed: 17148824]
8. Jezzard P, Balaban RS. Correction for geometric distortion in echo planar images from B0 field variations. Magn Reson Med. 1995;34(1):65–73. doi:10.1002/mrm.1910340111 [PubMed: 7674900]
9. Belov A, Bushuev V, Emelianov M, et al. Passive Shimming of the Superconducting Magnet for MRI. IEEE Trans Appl Supercond. 1995;5(2):679–681. doi:10.1109/77.402639
10. Liu F, Zhu J, Xia L, Crozier S. A hybrid field-harmonics approach for passive shimming design in MRI. IEEE Trans Appl Supercond. 2011;21(2):60–67. doi:10.1109/TASC.2011.2112358
11. Kong X, Zhu M, Xia L, et al. A novel passive shimming method for the correction of magnetic fields above the patient bed in MRI. J Magn Reson. 2015;257:64–69. doi:10.1016/j.jmr.2015.05.004 [PubMed: 26073600]

12. Wilson JL, Jenkinson M, Jezzard P. Optimization of static field homogeneity in human brain using diamagnetic passive shims. Magn Reson Med. 2002;48(5):906–914. doi:10.1002/mrm.10298 [PubMed: 12418007]
13. Wilson JL, Jezzard P. Utilization of an Intra-Oral Diamagnetic Passive Shim in Functional MRI of the Inferior Frontal Cortex. Magn Reson Med. 2003;50(5):1089–1094. doi:10.1002/mrm.10626 [PubMed: 14587020]
14. Cusack R, Russell B, Cox SML, De Panfilis C, Schwarzbauer C, Ansorge R. An evaluation of the use of passive shimming to improve frontal sensitivity in fMRI. Neuroimage. 2005;24(1):82–91. doi:10.1016/j.neuroimage.2004.08.029 [PubMed: 15588599]
15. Koch KM, Brown PB, Rothman DL, de Graaf RA. Adjustable Subject-Specific Passive Shims using Optimized Distributions of Bismuth and Zirconium. In: Int. Soc. Magn. Res. Med Vol 972. 2006:519.
16. Yang S, Kim H, Ghim MO, Lee BU, Kim DH. Local in vivo shimming using adaptive passive shim positioning. Magn Reson Imaging. 2011;29(3):401–407. doi:10.1016/j.mri.2010.10.004 [PubMed: 21216551]
17. Qu H, Wang Y, Niu C, Liu Y, Wang Q. A Novel Strategy and Test of Passive Shimming for Multi-Volumes in Cylindrical MRI Scanner. IEEE Trans Magn. 2020;56(2). doi:10.1109/TMAG.2019.2956666
18. Qu H, Niu C, Wang Y, Wang Q, Xia L, Liu F. The Optimal Target Magnetic Field Method for Passive Shimming in MRI. J Supercond Nov Magn. 2020;33(3):867–875. doi:10.1007/s10948-019-05241-2
19. Niu C, Tang F, Wang Q, Liu F. A Novel Active Shim Coil Design Scheme for the Effective Imaging Region above the Patient Bed in MRI. J Supercond Nov Magn. 2022;35(6):1685–1691. doi:10.1007/s10948-022-06249-x
20. Juchem C, Muller-Bierl B, Schick F, Logothetis NK, Pfeuffer J. Combined passive and active shimming for in vivo MR spectroscopy at high magnetic fields. J Magn Reson. 2006;183(2):278–289. doi:10.1016/j.jmr.2006.09.002 [PubMed: 17011219]
21. Biber S, Wohlfarth K, Kirsch J, Schmidt A. Design of a local shim coil to improve B0 homogeneity in the cervical spine region. In: Proceedings of the 20th Annual Meeting of ISMRM, Melbourne, Australia. Vol 2746. 2012.
22. Porter DA, Biber S, Kaarmann N, Wohlfarth K. Diffusion-Weighted Imaging of the Spine Using Readout-Segmented EPI and Local B0 Shimming. In: Proc. Intl. Soc. Mag. Reson. Med. Vol 22. 2014:1711.
23. Juchem C, Umesh Rudrapatna S, Nixon TW, de Graaf RA. Dynamic multi-coil technique (DYNAMITE) shimming for echo-planar imaging of the human brain at 7 Tesla. Neuroimage. 2015;105:462–472. doi:10.1016/j.neuroimage.2014.11.011 [PubMed: 25462795]
24. Stockmann JP, Witzel T, Keil B, et al. A 32-channel combined RF and B0 shim array for 3T brain imaging. Magn Reson Med. 2016;75(1):441–451. doi:10.1002/mrm.25587 [PubMed: 25689977]
25. Stockmann JP, Wald LL. In vivo B0 field shimming methods for MRI at 7 T. Neuroimage. 2018;168(June 2017):71–87. doi:10.1016/j.neuroimage.2017.06.013 [PubMed: 28602943]
26. Gao Y, Mareyam A, Sun Y, et al. A 16-channel AC/DC array coil for anesthetized monkey whole-brain imaging at 7T. Neuroimage. 2020;207(November 2019):116396. doi:10.1016/j.neuroimage.2019.116396 [PubMed: 31778818]
27. Stockmann JP, Arango NS, Witzel T, et al. A 31-channel integrated "AC/DC" B0 shim and radiofrequency receive array coil for improved 7T MRI. Magn Reson Med. 2022;87(2):1074–1092. doi:10.1002/mrm.29022 [PubMed: 34632626]
28. Liao C, Stockmann J, Tian Q, et al. High-fidelity, high-isotropic-resolution diffusion imaging through gSlider acquisition with B1+ and T1 corrections and integrated ΔB0/Rx shim array. Magn Reson Med. 2020;83(1):56–67. doi:10.1002/mrm.27899 [PubMed: 31373048]
29. Han H, Song AW, Truong TK. Integrated parallel reception, excitation, and shimming (iPRES). Magn Reson Med. 2013;70(1):241–247. doi:10.1002/mrm.24766 [PubMed: 23629974]
30. Juchem C, Nixon TW, McIntyre S, Boer VO, Rothman DL, De Graaf RA. Dynamic multi-coil shimming of the human brain at 7 T. J Magn Reson. 2011;212(2):280–288. doi:10.1016/j.jmr.2011.07.005 [PubMed: 21824794]

31. Jesmanowicz A. Method for Shimming a Static Magnetic Field in a Local MRI Coil. 2001;1(12).
32. Ren ZH, Stockmann JP, Dewdney A, Lee RF. Hybrid Active and Passive Local Shimming (HAPLS) for Two-region Magnetic Resonance Imaging (MRI). In: In Proceedings of the 30th Annual Meeting of ISMRM. 2021:3327.
33. Ren ZH, Mu WC, Huang SY. Design and Optimization of a Ring-Pair Permanent Magnet Array for Head Imaging in a Low-Field Portable MRI System. IEEE Trans Magn. 2019;55(1):1–8. doi:10.1109/TMAG.2018.2876679
34. Ren ZH, Gong J, Huang SY. An Irregular-Shaped Inward-Outward Ring-Pair Magnet Array with a Monotonic Field Gradient for 2D Head Imaging in Low-Field Portable MRI. IEEE Access. 2019;7:48715–48724. doi:10.1109/ACCESS.2019.2909834
35. Furlani EP. Permanent Magnet and Electromechanical Devices. Academic press; 2001. doi:10.1016/b978-0-12-269951-1.x5000-1
36. Sivanandam SN, Deepa SN. Genetic algorithms. In: Introduction to Genetic Algorithms. Springer; 2008:15–37.
37. Arango N, Stockmann J, Witzel T, Wald L, White J. Low-cost, open-source, flexible current feedback-controlled coil driver circuit for matrix B0 shim coils and related applications. In: Proceedings of the ISMRM. 2016:1157.
38. Current driver:Current driver - RF Coil Lab. https://rflab.martinos.org/index.php?title=Current_driver:Current_driver. Accessed April 6, 2022.
39. Seeber DA, Jevtic J, Menon A. Floating shield current suppression trap. Concepts Magn Reson Part B Magn Reson Eng. 2004;21(1):26–31. doi:10.1002/cmr.b.20008
40. Simon MD, Heflinger LO, Geim AK. Diamagnetically stabilized magnet levitation. Am J Phys. 2001;69(6):702–713. doi:10.1119/1.1375157
41. Hancu I, Govenkar A, Lenkinski RE, Lee SK. On shimming approaches in 3T breast MRI. Magn Reson Med. 2013;69(3):862–867. doi:10.1002/mrm.24307 [PubMed: 22556115]
42. Han M, Cunningham CH, Pauly JM, Daniel BL, Hargreaves BA. Homogenous fat suppression for bilateral breast imaging using independent shims. Magn Reson Med. 2014;71(4):1511–1517. doi:10.1002/mrm.24803 [PubMed: 23821305]

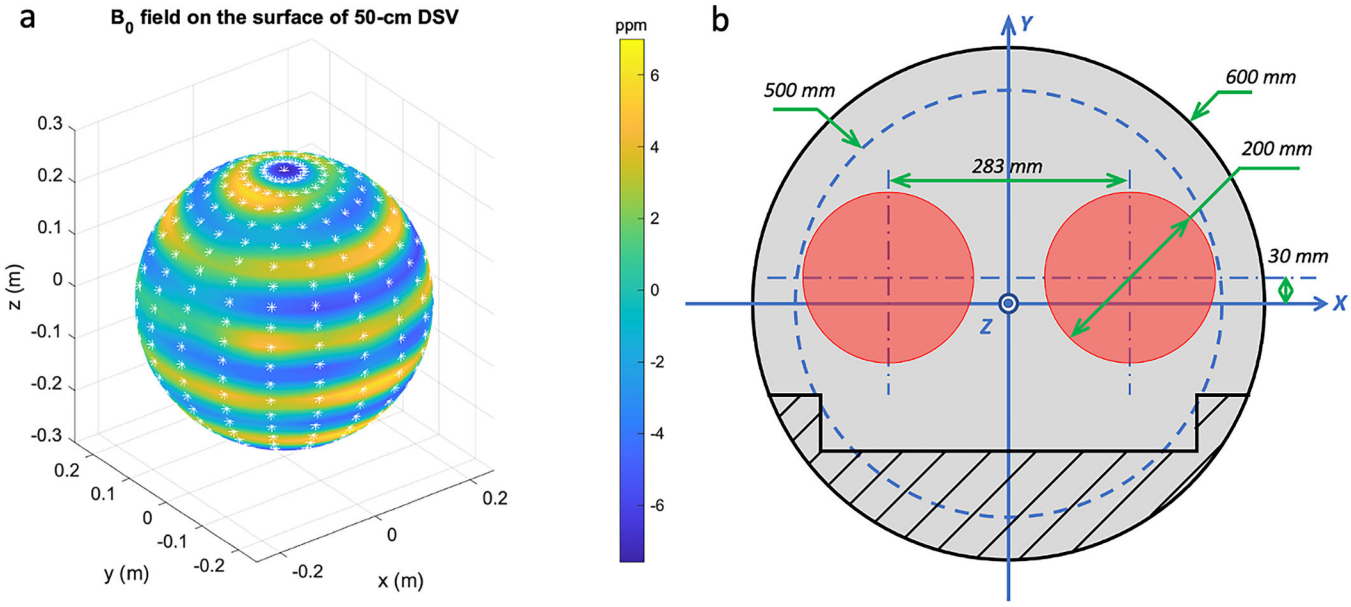

Figure 1.

(a) The plot of the magnetic field on the surface of the 50-cm DSV, and white star signs depict the positions of the field probe magnetometer used to take the measurement. (b) The location and dimension of bi-focal regions targeted for shimming two heads at the same time. The left region (−x side) and the right region (+x side) will be referred to as sub-FOV1 and sub-FOV2 in this paper, respectively.

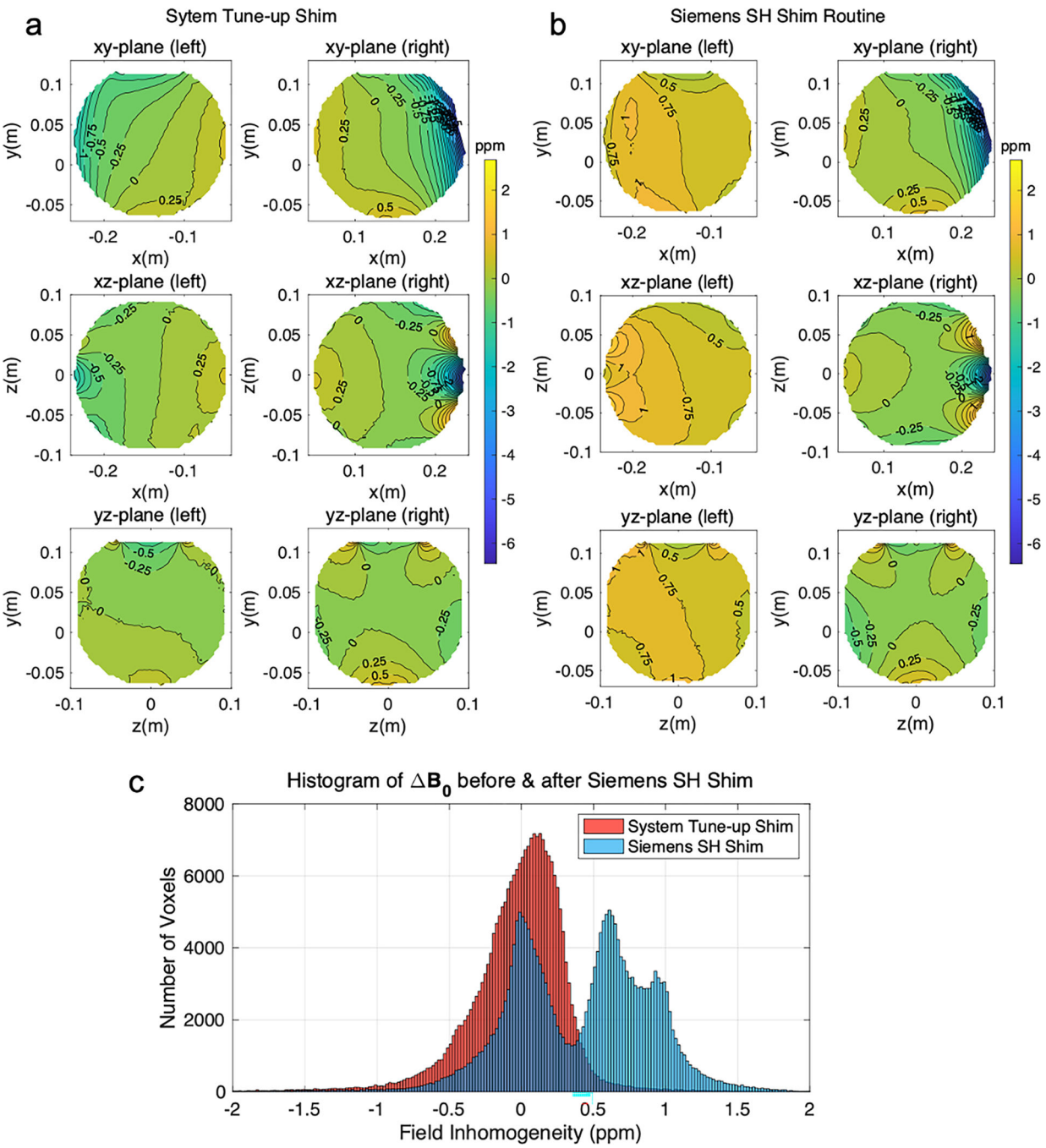

Figure 2.

Acquired B_0 field maps inside the paired 20-cm spherical phantoms in three central planes with system tune-up shim setting and after automatic SH shimming are shown in (a) and (b), respectively. (c) The histogram plot of the ΔB_0 field distribution with system tune-up shimming and automatic SH shimming.

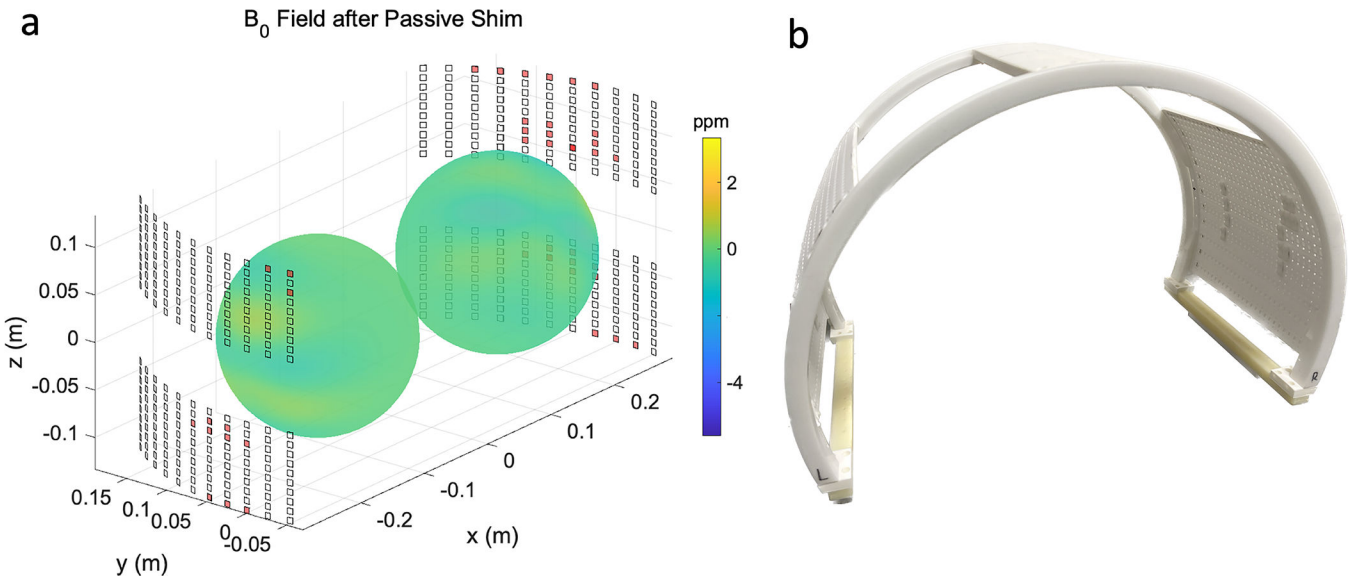

Figure 3.

(a) B_0 field on the spherical surface of two sub-FOVs after passive shim is shown. The optimized chip distribution (red cuboids) is also illustrated, and transparent chip blocks depict that no chips are placed there based on the optimization results. (b) The assembly of the passive shim fixture with shim chips affixed.

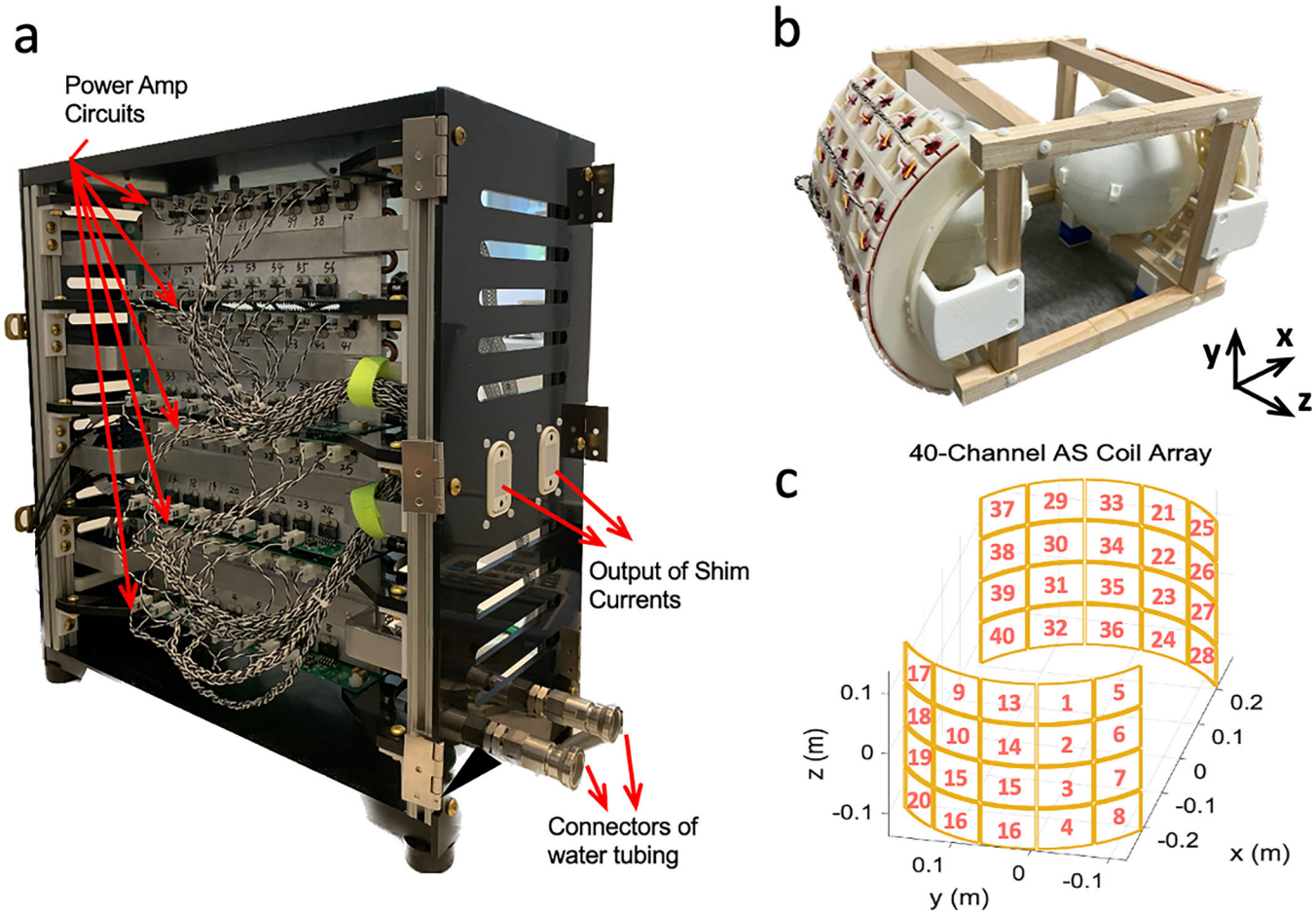

Figure 4.

(a) The 64-channel shim current supply system. (b) The 40-channel bilateral active shim coils with home-made phantom filled with $CuSO_4$ solution. (c) The 40-channel active shim coil array are depicted, and each of the coil loop is labelled.

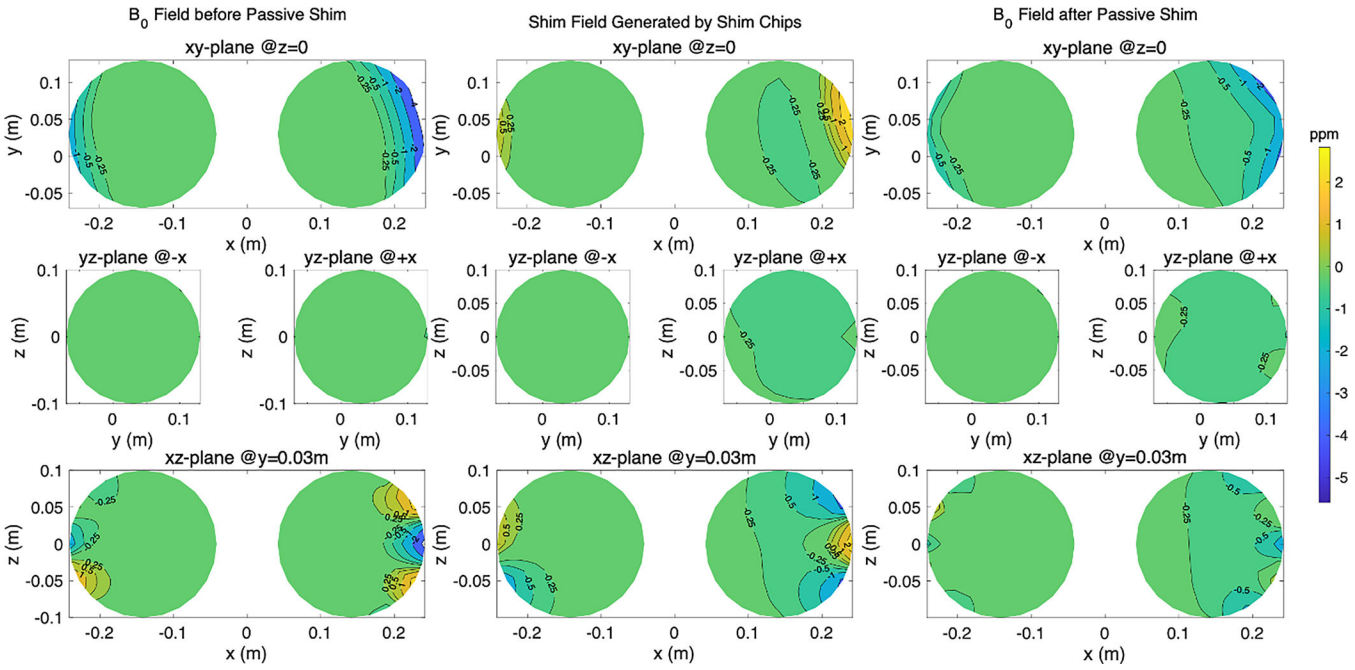

Figure 5.

The background B_0 field, the shim field generated by passive shim chips, and the B_0 field after applying PS in three central planes within both sub-FOVs are shown.

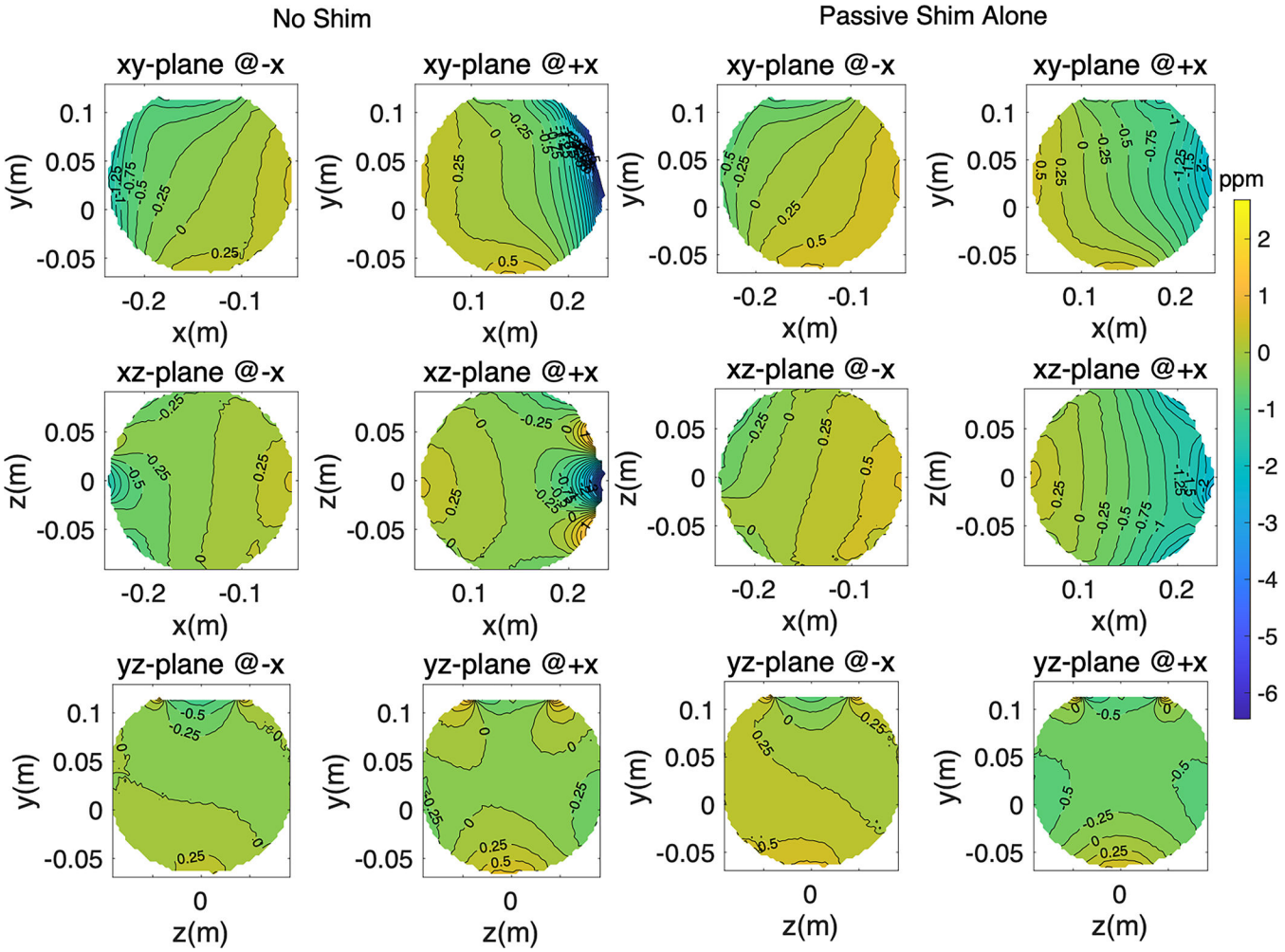

Figure 6.

The B_0 field before and after applying the passive shim are shown in three central planes, respectively.

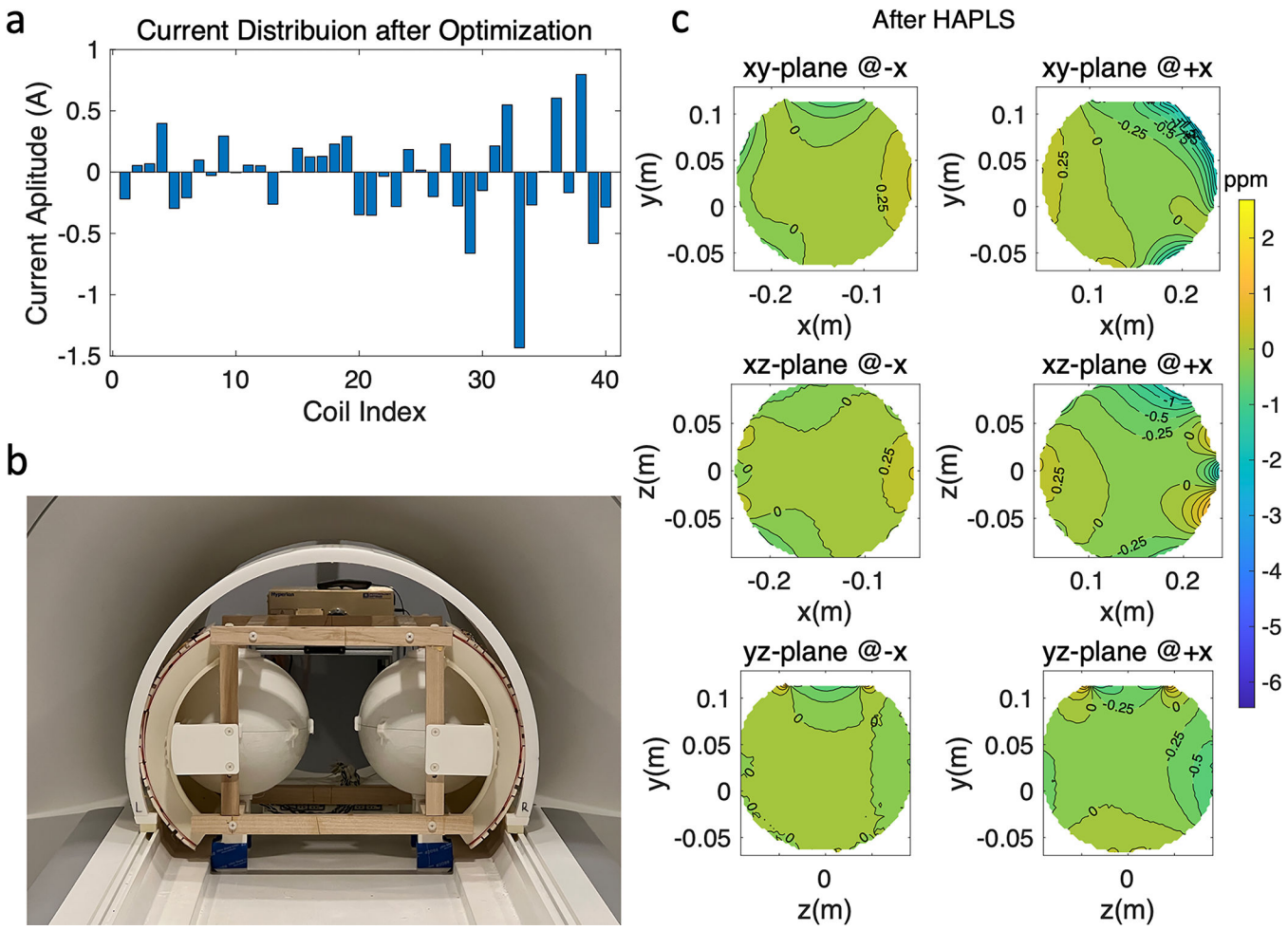

Figure 7.

(a) The current distribution for 40-channel active shim coils after optimization. (b) The setup in the scanner to perform HAPLS. (c) The field map within two phantoms after applying HAPLS.

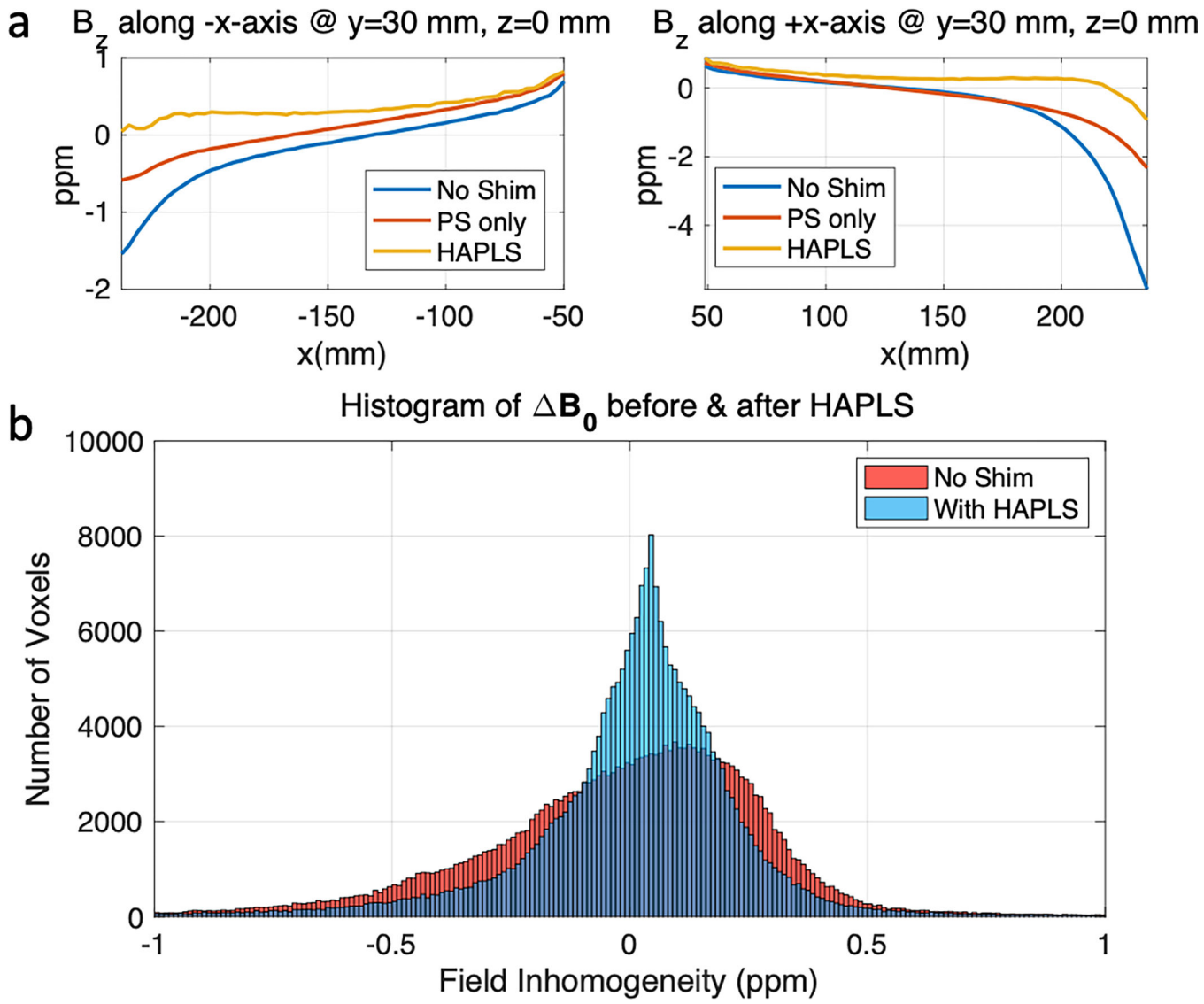

Figure 8.

(a) B_Z field along the x-axis @ y = 30 mm in both sub-FOVs is shown. (b) Histogram plot of field inhomogeneity within both sub-FOVs before (red) and after (blue) applying HAPLS.

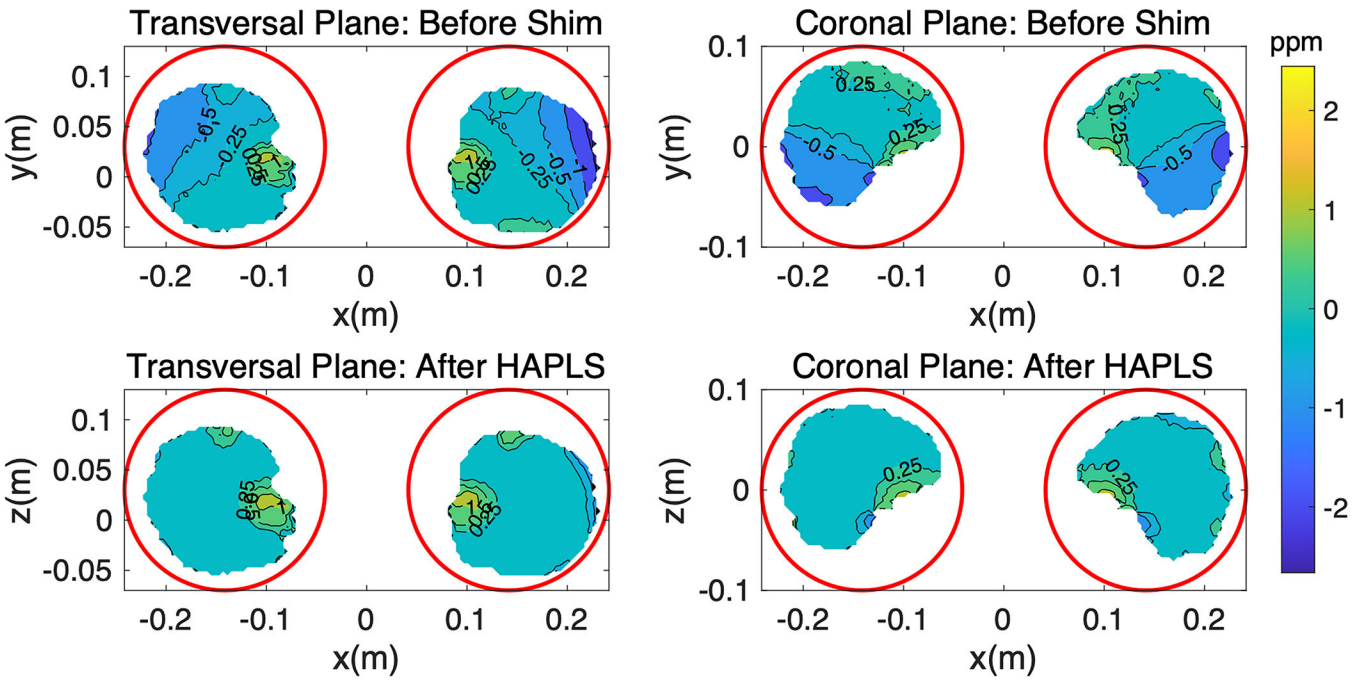

Figure 9.

The B_0 field in two brains within two targeted imaging regions before and after applying HAPLS. The red circles depict two targeted 20-cm imaging regions.

Table 1.

The location and dimension of the optimized shim chip/chip stack array.

	+X Side (Thickness Unit: mm)											−X Side (Thickness Unit: mm)									
	350°	355°	0°	5°	10°	15°	20°	25°	30°	35°	40°	140°	145°	150°	155°	160°	165°	170°	175°	180°	185°
130	0	0	0	0	0	0	0	0	0	0.05	0.10	0	0	0.25	0.05	0.05	0.05	0.10	0.05	0	0
120	0	0	0	0	0	0	0	0	0	0	0	0	0	0	0	0	0	0	0	0	0
110	0	0	0	0	0	0	0	0	0	0	0.05	0	0	0	0	0	0	0	0	0	0
100	0	0	0	0	0	0	0	0	0	0	0	0	0	0	0	0	0	0	0	0	0
90	0	0	0	0	0	0	0	0	0	0	0	0	0	0	0	0	0	0	0	0	0
80	0	0	0	0	0	0	0	0	0	0	0	0	0	0	0	0.05	0.10	0	0.05	0	0
70	0	0	0	0	0	0	0	0	0	0	0	0	0	0	0	0.05	0.05	0	0.05	0	0
60	0	0	0	0	0	0	0	0	0	0	0	0	0	0	0	0.05	0.05	0.35	0.05	0.05	0
50	0	0	0	0	0	0	0	0	0	0	0	0	0	0	0	0	0	0	0	0	0
40	0	0	0	0	0	0	0	0	0	0	0	0	0	0	0	0	0	0	0	0	0
−40	0	0	0	0	0	0	0	0	0	0	0	0	0	0	0	0	0	0	0	0	0
−50	0	0	0	0	0	0	0.05	0.05	0	0	0	0	0	0	0	0	0.05	0.05	0	0	0
−60	0	0	0	0	0	0.05	0.05	0.10	0.05	0	0	0	0	0	0	0.15	0.35	0.10	0.05	0	0
−70	0	0	0	0	0	0	0	0	0	0	0	0	0	0	0	0	0	0.05	0.05	0	0
−80	0	0	0	0	0	0	0	0	0	0	0	0	0	0	0	0	0	0	0	0	0
−90	0	0	0	0	0	0	0	0	0	0	0	0	0	0	0	0	0	0	0	0	0
−100	0	0	0	0	0	0	0	0	0	0	0	0	0	0	0	0	0	0	0	0	0
−110	0	0	0	0	0	0	0	0	0	0	0	0	0	0	0	0	0	0	0	0	0
−120	0	0	0	0	0	0	0	0	0	0	0	0	0	0	0	0	0	0	0	0	0
−130	0	0	0	0	0	0	0.05	0.05	0.05	0	0	0	0	0	0	0	0	0	0.10	0.05	0.05

Z (mm)